Article   https://doi.org/10.1038/s41467-025-63902-4

Directing selective solvent presentations at electrochemical interfaces to enable initially anode-free sodium metal batteries

Qianli Xing [1], Jung Min Lee [2], Ziqi Yang[3], Reid C. Van Lehn[2,3] & Fang Liu [1,2] ✉

Initially anode-free sodium metal batteries offer a high energy density at lower costs than lithium-ion batteries, making them a promising alternative for portable electronics, transportation, and power grids. However, side reactions at the electrode/electrolyte interface hinder their practical applications. Our study reveals that negative electrode stability is primarily influenced by the solvents in the cation's first solvation shell, whereas positive electrode stability is dictated by weakly bonded solvents. Based on this insight, we introduce an electrolyte design strategy to selectively direct 2-methyltetrahydrofuran to the Na metal electrode and tetrahydrofuran to the $NaNi_{1/3}Fe_{1/3}Mn_{1/3}O_2$ positive electrode interface, optimizing stability for both electrodes. With this tailored electrolyte, we achieve an average Coulombic efficiency of 99.91% in Na||Cu cells for 400 cycles at $1\,mA/cm^2$ with $1\,mAh/cm^2$ and demonstrate stable Na plating/stripping for 5000 h at $2\,mA/cm^2$ with $2\,mAh/cm^2$ in Na||Na cells. Furthermore, an initially anode-free sodium metal battery with a positive electrode active material loading of $14.05\,mg\,cm^{-2}$ retains 90.9% of its capacity over 150 cycles at $110\,mA\,g^{-1}$, even after aging, underscoring its potential for practical applications.

Initially anode-free sodium metal batteries exhibit significant potential for delivering energy densities that are either higher or comparable to lithium-ion batteries, both volumetrically (638 Wh/L for Al||$NaNi_{0.33}Mn_{0.66}O_2$ *vs.* 650 Wh/L for Graphite||$LiNi_{0.8}Co_{0.1}Mn_{0.1}O_2$ and 383 Wh/L for Graphite||$LiFePO_4$) and gravimetrically (269 Wh/kg for Al||$NaNi_{0.33}Mn_{0.66}O_2$ *vs.* 243 Wh/kg for Graphite||$LiNi_{0.8}Co_{0.1}Mn_{0.1}O_2$ and 139 Wh/kg for Graphite||$LiFePO_4$)[1]. This promising performance, along with their ability to eliminate dependence on lithium and cobalt resources, positions sodium metal batteries as attractive candidates for a range of applications, including portable electronics, electric vehicles, and power grids[2,3]. However, despite these advantages, their practical implementation is primarily constrained by their limited cycle life[4] and calendar life[5], which must be addressed to fully unlock their potential.

To enable the practical application of initially anode-free sodium metal batteries and achieve their high energy density with a minimal self-discharge rate, the electrolyte must demonstrate good electro-chemical stability at both electrodes across wide voltage windows and over extended timeframes. Achieving these criteria with a single solvent remains extremely challenging, especially over wide temperature ranges[6,7]. A common strategy in electrolyte design involves using solvent mixtures to fine-tune their electrochemical properties[8–10]. While weak correlations between electrolyte composition, solvation structure, and electrochemical behavior have been identified[11], the precise distribution of solvents within different cation solvation structures, such as aggregates (AGG), contact ion pairs (CIP), and solvent-separated ion pairs (SSIP), and their influence on electrochemical behavior at both electrodes, remain poorly understood. This knowledge gap hinders the rational design of electrolytes, thereby limiting

---

[1]Department of Materials Science and Engineering, University of Wisconsin-Madison, Madison, WI, USA. [2]Department of Chemical and Biological Engineering, University of Wisconsin-Madison, Madison, WI, USA. [3]Department of Chemistry, University of Wisconsin-Madison, Madison, WI, USA.
✉e-mail: fang.liu3@wisc.edu

the widespread adoption of sodium metal batteries as well as other advanced metal battery technologies such as lithium, aluminum, magnesium, and beyond[12–15].

In this study, we present a electrolyte design strategy to address these challenges by directing the selective and distinct presentation of solvents at the negative electrode and positive electrode interfaces to achieve optimal stability at both electrodes. Our approach fundamentally separates the determinants of electrode stability: negative electrode stability is primarily determined by the solvents in the cation's first solvation shell, while positive electrode stability is governed by the presence of free or weakly bonded solvents. To validate this electrolyte design concept, we chose a solvent mixture of tetrahydrofuran (THF) and 2-methyltetrahydrofuran (2-MeTHF) with distinct electrochemical stabilities as a model system to enable initially anode-free sodium metal full cells. Molecular dynamics simulations were employed to investigate the distribution of these two solvents within the cation solvation structure. The results revealed a selective enrichment of the negative electrode-stabilizing 2-MeTHF within the cation's first solvation shell across AGGs, CIPs, and SSIPs, contributing to enhanced negative electrode stability. In contrast, the positive electrode-stabilizing THF was preferentially enriched in a free or weakly bonded state, making it readily available to solvate newly formed cations. This tailored solvent distribution enables the selective and distinct presentations of the two electrolyte components at the negative and positive electrodes during battery operation, effectively harnessing their respective electrochemical stabilities to achieve optimal electrochemical performance. At the negative electrode, the electrolyte achieves high Na plating/stripping Coulombic efficiencies (CE) exceeding 99.91% at $22 \pm 1 °C$, with dramatically extended calendar life, retaining 81% of its capacity after 21 days. In Na||Na symmetric cells, the electrolyte shows a cycle life exceeding 5000 h under a current density of $2 \, mA/cm^2$, surpassing the performance of current state-of-the-art electrolytes for sodium metal batteries [Supplementary Tables 1, 2]. At the positive electrode, the electrolyte facilitates stable cycling of Na||NFM ($NaNi_{1/3}Fe_{1/3}Mn_{1/3}O_2$, mass loading = $14.05 \, mg/cm^2$) cells across a wide temperature range, with 77% capacity retention after 500 cycles at $22 \pm 1 °C$. Building on its stability at both electrodes, this electrolyte enables high-energy-density initially anode-free sodium metal batteries to deliver 90.9% and 84.8% of initial capacity over 150 cycles at $22 \pm 1 °C$ and 150 cycles at $-30 \pm 1 °C$ under lean electrolyte conditions, highlighting its potential for practical application. This selective solvent presentation strategy provides a rational framework for tailoring solvation structures to meet the distinct electrochemical requirements of both electrodes, paving the way for the advancement of initially anode-free metal batteries, particularly sodium and lithium-based systems.

Results

Designing electrolytes with tailored solvent distribution

The solvation structure of electrolytes plays a pivotal role in determining their electrochemical behaviors, yet solvation remains a highly intricate phenomenon due to the complex molecular interactions among cations, anions, and solvents. This complexity is further intensified by the dynamic generation and consumption of cations at the two electrodes during battery operation. A notable feature of a battery system is that the solvation and desolvation processes at the electrodes' surface are opposite. For instance, during the battery charging process, cation desolvation occurs at the negative electrode, while solvation takes place at the positive electrode. These solvation processes are reversed during the discharging process. Meanwhile, the SEI layer is primarily formed during the first charging process and the high voltages during charging dramatically accelerate side reactions, emphasizing the critical roles of cation desolvation at the negative electrode and solvation at the positive electrode. As a result, negative electrode stability is predominantly determined by the solvents present in the cation's first solvation shell. In contrast, positive electrode stability is largely influenced by free solvents that are not present within ion solvation shells, as they are uniquely suited to solvate the newly formed cations at the positive electrode surface during charging (Fig. 1). These distinct roles of solvent molecules at the negative and positive electrode highlight the importance of tailoring the solvent environment to achieve stability at both electrodes.

We selected THF and 2-MeTHF as a representative example to implement this electrolyte design concept of selective solvent presentations aimed at enabling initially anode-free sodium metal batteries. THF and 2-MeTHF have distinct electrochemical stabilities: 2-MeTHF demonstrates good electrochemical stability under reductive conditions[16], making it favorable for negative electrode interactions, while THF is more stable under oxidative conditions because of its lower highest occupied molecular orbital (HOMO) energy (Supplementary Table 3), rendering it suitable for the positive electrode environment. We hypothesize that negative electrode stability is determined by the solvent in the first solvation shell while positive electrode stability is governed by the weakly bonded solvent in the electrolyte. The salt concentration in these electrolytes was chosen based on the solubility of $NaPF_6$ in THF, 2-MeTHF and their mixture (Supplementary Fig. 1, Supplementary Note 1, Supplementary Table 4). The solvation structure of electrolytes composed of either solvent
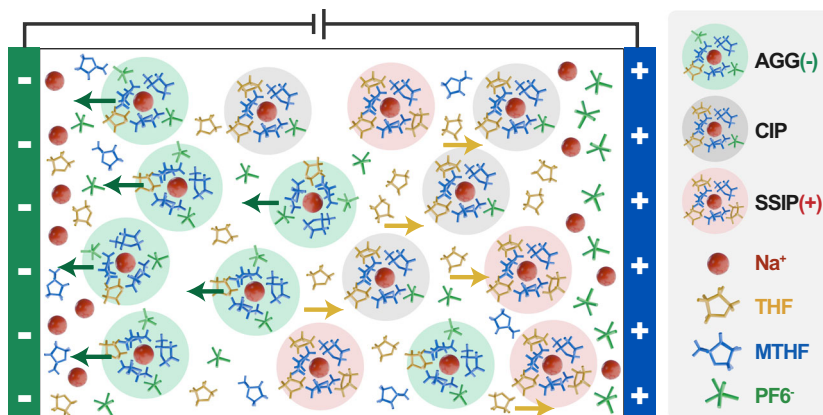

Fig. 1 | Electrolyte design strategy. Illustration of solvent distributions in the electrolyte during the battery charging process. The cation solvation shells are enriched in 2-MeTHF, which results in the generation of a stable Na|electrolyte interface under reductive conditions. Meanwhile, THF is weakly bonded to cations and accumulates on the positive electrode to prevent oxidation. The developed 1.8 M $NaPF_6$ in THF/2-MeTHF electrolyte promotes the formation of a selective solvent presentation at different electrochemical interfaces, collectively enhancing the reversibility and calendar life of the initially anode-free Na metal batteries.
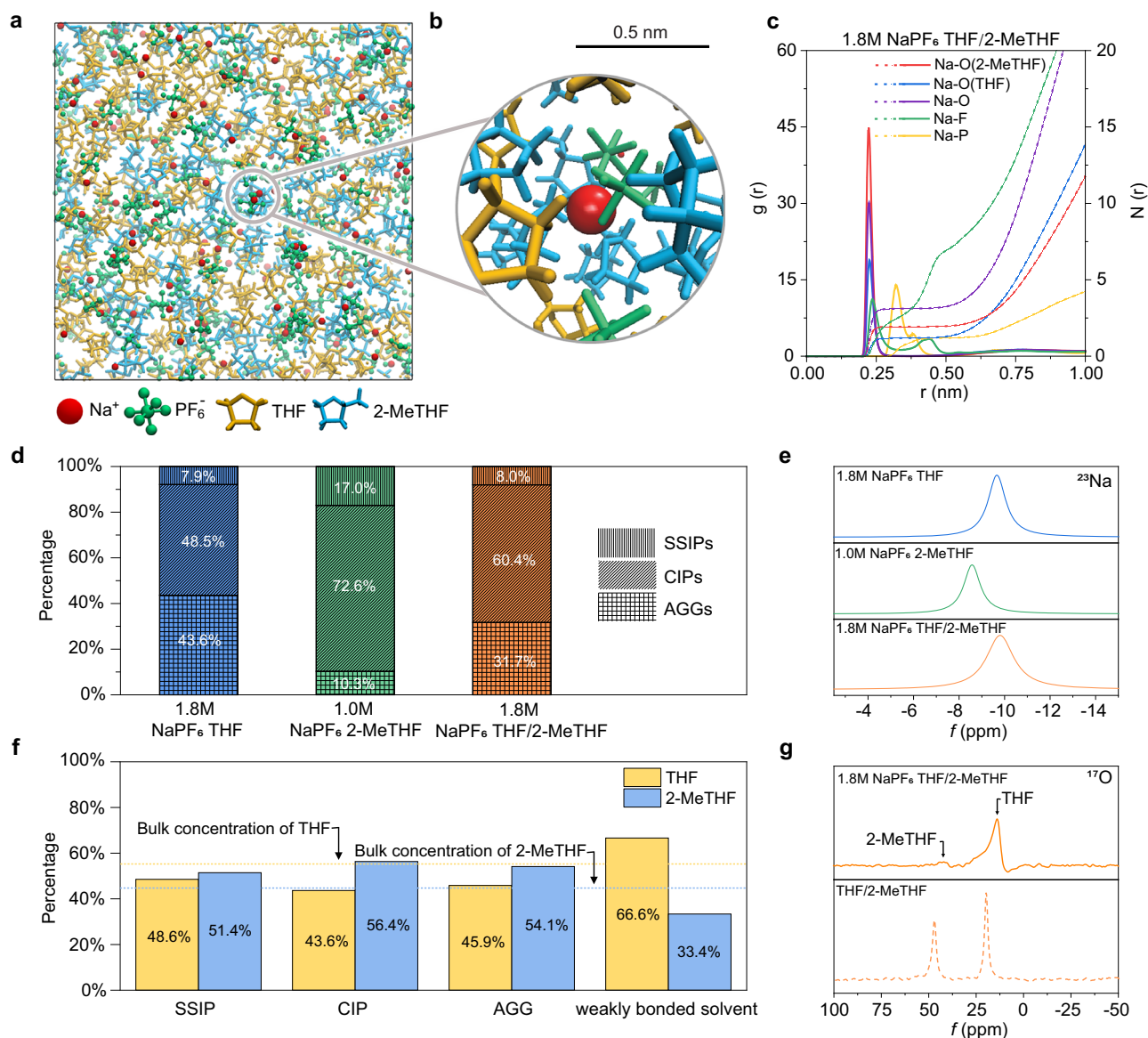
Fig. 2 | Solvation structure of electrolytes. a Snapshot of the MD simulation system for 1.8 M NaPF$_6$ in THF/2-MeTHF. **b** Snapshot of an example AGG solvation shell for the 1.8 M NaPF$_6$ in THF/2-MeTHF electrolyte. Only solvent molecules with an oxygen atom within 0.5 nm of the central Na$^+$ ion are shown. **c** Radial distribution function g(r) (solid lines) and coordination number N(r) (dotted lines) for 1.8 M NaPF$_6$ in THF/2-MeTHF. **d** Distribution of solvation shell types for single solvent and mixed-solvent systems from simulations. **e** NMR spectra of ^{23}Na in various investigated electrolytes. **f** Percentage of THF and 2-MeTHF for each solvation shell type

(SSIP: solvent-separated ion pairs, CIP: contact ion pairs, AGG: aggregates) for 1.8 M NaPF$_6$ in THF/2-MeTHF. The dotted lines indicate the percentage of each solvent species in the entire simulation system; solvation shells are consistently enriched in 2-MeTHF (larger columns than the dashed blue line) and depleted in THF (smaller columns than the dashed line). Free solvent indicates solvent molecules do not present in any first solvation shell. **g** NMR spectra of ^{17}O in the 1.8 M NaPF$_6$ in THF/2-MeTHF electrolyte and THF/2-MeTHF solvent.

individually or mixtures of the two solvents (v:v = 1:1) with 1 M or 1.8 M NaPF$_6$ were thus investigated using all-atom molecular dynamics (MD) simulations (Fig. 2a, b, Supplementary Fig. 2 and Supplementary Table 5), which have been utilized in prior studies to characterize solvation structures in electrolytes and complex solvent mixtures[17–19]. The results reveal that Na$^+$ and PF$_6^-$ ions are uniformly dispersed within all electrolytes, indicating well-distributed, ion-conducting environments.

To gain deeper insight into cation solvation structures, we analyzed the MD simulation data to compute Na$^+$ radial distribution functions (RDF) and coordination numbers (Supplementary Table 6). The RDF provides a quantitative measure of the spatial distribution of ions (i.e., Na$^+$ and PF$_6^-$) and solvent molecules relative to a central Na$^+$ ion, with values greater than 1 indicating enrichment relative to the

bulk concentration of a species. The coordination number reports the average number of solvent molecules and ions as a function of the distance from a central Na$^+$ ion. In all electrolytes (Fig. 2c, Supplementary Fig. 3), the distance between Na$^+$ and the oxygen (O) atom of the solvent molecules (i.e., the distance corresponding to the maximum of the Na$^+$-O RDF) is similar to the distance between Na$^+$ and the fluorine (F) atoms of PF$_6^-$, but this distance is notably shorter than the distance between Na$^+$ and the phosphorus (P) atom. This observation can be attributed to the structure of PF$_6^-$, where the spatial arrangement of phosphorus (P) and fluorine (F) atoms creates a gap between their first RDF peaks. This structural feature facilitates closer interactions between Na$^+$ and the F and O atoms, increasing their likelihood of being dragged to the reaction site and, if decomposed, being incorporated into the solid electrolyte interphase (SEI). In the electrolytes

containing solvent mixtures, the first peak of the RDF for the O atom is primarily attributed to 2-MeTHF for both 1 M and 1.8 M NaPF$_6$, indicating that Na$^+$−2-MeTHF interactions are stronger than Na$^+$-THF interactions. Consistently, the RDFs of electrolytes with single solvents (Supplementary Fig. 3) also show that the first peak of the O atom is higher in 2-MeTHF compared to THF, despite the lower salt concentration in 2-MeTHF due to solubility limitations. This difference originates from the differences in solvation affinity between Na$^+$, PF$_6^-$, and these solvent molecules. To quantify solvation affinity, we performed solvation free energy calculations which revealed that the presence of 2-MeTHF leads to a lower solvation free energy (higher solvation affinity) for Na$^+$, while THF increases the solvation affinity for PF$_6^-$ (Supplementary Tables 10, 11, Supplementary Note 2).

The differences in solvation affinity also influence the ion pairing configurations for Na$^+$ and PF$_6^-$ in these electrolytes. Based on the simulation analysis of the number of phosphorus (P) atoms within a specified distance cutoff (0.5 nm) of Na$^+$, ion clusters are categorized as SSIPs (P = 0), CIPs (P = 1), and AGGs (P ≥ 2) (Supplementary Fig. 4). Figure. 2d quantifies the distribution of these ion clusters in electrolytes containing individual solvents and the solvent mixture. The 1.8 M NaPF$_6$ salt concentration in THF system exhibits a strong tendency for ion aggregation (the ratio of CIPs:AGGs = 1.11), while 1 M NaPF$_6$ in 2-MeTHF favors the formation of CIPs (CIPs:AGGs = 7.05) and SSIPs. The solvent mixture with 1.8 M NaPF$_6$ in THF/2-MeTHF significantly promotes the formation of AGGs compared to 2-MeTHF (CIPs:AGGs = 1.90), with the percentage of AGGs (31.7%) approaching the values in the THF system (43.6%). To compare to the simulation results, we also used Raman spectroscopy, which probes the stretching vibration of solvated PF$_6^-$ at 738.8 cm^{-1}, to reveal a similar trend regarding ion pairing and aggregation (Supplementary Fig. 5). The results indicate a significantly higher percentage of AGGs in 1.8 M NaPF$_6$ in THF (39.7%) and THF/2-MeTHF (31.4%), both of which are considerably higher compared to the 1 M NaPF$_6$ in 2-MeTHF (20.3%), which is consistent with the simulations. Consistently, the ^{23}Na nuclear magnetic resonance (NMR) spectra of these electrolytes further reveal that the more electron-dense PF$_6^-$ anion is introduced into the first solvation shell in 1.8 M NaPF$_6$ in THF and THF/2-MeTHF electrolytes, as indicated by an upfield (more negative) shift compared to 1.0 M NaPF$_6$ in 2-MeTHF (Fig. 2e)[20]. Meanwhile, the ^{23}Na NMR spectrum of 1.8 M NaPF$_6$ in THF/2-MeTHF exhibits a slightly wider peak, suggesting a more diverse solvation structure for Na$^+$[21].

To identify the distribution of THF and 2-MeTHF in the solvation structure, we further analyzed the MD simulation data to quantify the solvent composition within the first solvation shell of Na$^+$ in 1.8 M NaPF$_6$ in the THF/2-MeTHF electrolyte (Fig. 2f, Supplementary Table 12). 2-MeTHF is enriched in AGGs (representing 54.1% of the solvent molecules), CIPs (56.4%), and SSIPs (51.5%), all values exceeding its bulk percentage (44.8%). Conversely, THF is depleted in solvation shells and represents a higher percentage of solvent molecules that are not within a cation solvation shell (labeled free solvent in Fig. 2f) than the overall percentage of THF in the mixture, which indicates that THF predominantly exists in a more weakly bonded state that could play a critical role in solvating newly formed cations during electrochemical reactions[22]. Together, this simulation analysis indicates that there is preferential solvation of Na$^+$ by 2-MeTHF over THF. To further validate the generality of these findings, we also performed additional MD simulations for 1.8 M NaPF$_6$ in THF/2-MeTHF (3:7 and 7:3) mixtures. These systems exhibited similar trends in solvation structure, with 2-MeTHF preferentially coordinated near Na$^+$ and THF predominantly residing in the bulk (Supplementary Tables 13 and 14, Supplementary Figs. 6–8). Notably, the 3:7 mixture exhibited the strongest enrichment of 2-MeTHF within the solvation shell but a relatively low level of ion aggregation, whereas the 7:3 system had more aggregates but lower 2-MeTHF availability. Furthermore, we evaluated the Coulombic efficiency of Na deposition and stripping in

two other mixture electrolytes with different volume ratios (i.e., 3:7 and 7:3 v:v) between THF and 2-MeTHF. We observed that the cells with 1.8 M NaPF$_6$ in THF/2-MeTHF (v:v = 1:1) electrolyte exhibited the highest CE over 99.99%. In sharp contrast, the cells with the other two electrolytes demonstrated significantly lower CEs of <99.7% (Supplementary Fig. 9). These results support the idea that the 5:5 (i.e., 1:1) mixture represents a balanced solvation environment. The preferential solvation is also evident in the experimentally determined ^{17}O NMR spectrum (Fig. 2g). THF and 2-MeTHF exhibit distinct ^{17}O chemical shifts, at 19.5 ppm for THF and 47.0 ppm for 2-MeTHF, where the peak intensity corresponds to the concentration of lone-pair electrons on the oxygen atoms in the solvent molecules. When 1.8 M NaPF$_6$ salt is introduced to the mixed solvent, both peaks in the ^{17}O NMR spectrum exhibit an upfield shift, broadening, and significantly lower intensities. These changes reflect the emergence of diverse solvation environments due to the interaction of the solvents with Na$^+$ and PF$_6^-$ ions. Notably, the peak intensity for 2-MeTHF nearly drops to zero, indicating that almost all free 2-MeTHF molecules are tightly bonded with Na$^+$ and PF$_6^-$ ions[23]. This observation is consistent with the MD simulation results (Fig. 2f), which confirm that 2-MeTHF dominates the first solvation shell of Na$^+$. Considering the distinct electrochemical stabilities of the two solvents−2-MeTHF being stable under reductive conditions and THF under oxidative environments−this naturally formed solvent distribution is ideally suited for ensuring optimal electrochemical stability at both electrodes.

Influence of solvation structure on negative electrode stability

To illustrate how the solvent distribution in the solvation structure influences electrochemical performance in Na metal batteries, we conducted a comprehensive series of electrochemical tests using a mixed-solvent system (1.8 M NaPF$_6$ in THF/2-MeTHF), compared with single solvent systems (1.8 M NaPF$_6$ in THF, 1 M NaPF$_6$ in 2-MeTHF). The electrochemical stability and kinetics of the electrolytes against Na were assessed using cyclic voltammetry (CV). All electrolytes (1.8 M NaPF$_6$ in THF, 1 M NaPF$_6$ in 2-MeTHF, 1.8 M NaPF$_6$ in THF/2-MeTHF) demonstrate decent stability against Na under a scan rate of 5 mV/s, as indicated by nearly symmetric Na deposition and stripping peaks (Fig. 3a). However, variations in peak currents and overpotentials were observed, reflecting significant differences in their electrochemical kinetics[24]. The results show that the electrochemical kinetics at the Na negative electrode is significantly faster in 1.8 M NaPF$_6$ in THF, followed by 1.8 M NaPF$_6$ in THF/2-MeTHF, and are slowest in 1 M NaPF$_6$ in 2-MeTHF. This variation is attributed not only to differences in ionic conductivity (Fig. 3b) but also to the content of AGGs in the electrolytes (Fig. 2d), which follows the trend 1.8 M NaPF$_6$ in THF > 1.8 M NaPF$_6$ in THF/2-MeTHF > 1 M NaPF$_6$ in 2-MeTHF.

The electrochemical behaviors and stability of these electrolytes Na become more pronounced during Na deposition and stripping under a constant current of 1 mA/cm^2 over long-term cycling. Consistent with the CV results, the electrodeposition of Na in 1.8 M NaPF$_6$ in THF and 1.8 M NaPF$_6$ in THF/2-MeTHF electrolytes exhibits lower electrochemical overpotentials compared to that in 1 M NaPF$_6$ in 2-MeTHF. However, a notable limitation emerges in 1.8 M NaPF$_6$ in THF, where THF demonstrates poor stability against Na. This is reflected in a very low initial Coulombic efficiency (ICE) of 74.31%, which is significantly lower than the 93% ICE achieved by the other two electrolytes containing 2-MeTHF (Fig. 3c). Additionally, fluctuations in voltages and CE were frequently observed in the charge-discharge curves of 1.8 M NaPF$_6$ in the THF electrolyte, particularly after 100 cycles, indicating occurrences of soft shorting (Fig. 3d, e). On the other hand, while the 1 M NaPF$_6$ 2-MeTHF electrolyte initially demonstrates good electrochemical stability, its CE drops sharply to 21.39% after only 50 cycles (Fig. 3d, f). This rapid decline is likely due to the limited ionic conductivity and amount of AGGs in the system, which results in insufficient transport of active species to the electrode
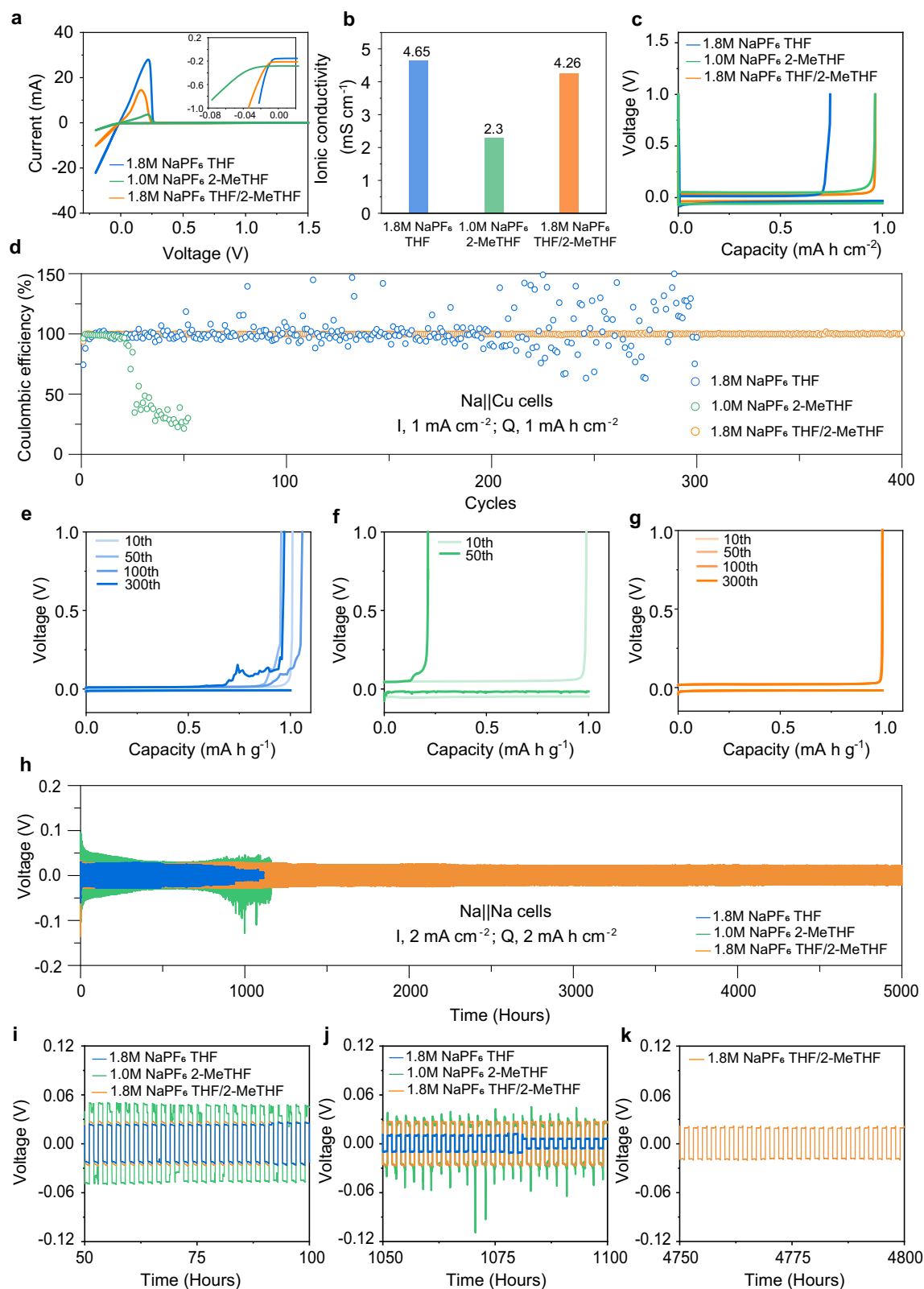
Fig. 3 | Na plating/stripping behaviors in different electrolytes. a CV curves of the Na||Cu cells at 5 mV/s scan rate in various electrolytes. **b** Ionic conductivity of different electrolytes. **c** 1st cycle voltage profile of Cu||Na half cells. **d** Coulombic efficiency of Na plating/stripping and the corresponding voltage profiles in **e.** 1.8 M NaPF$_6$ in THF, **f.** 1 M NaPF$_6$ in 2-MeTHF and **g.** 1.8 M NaPF$_6$ in THF /2-MeTHF electrolyte at various cycles as indicated in the legend. **h** Na plating/stripping stability of Na||Na symmetric cell and (**i**–**k**). corresponding zoomed-in plots.

surface and unstable SEI layer, ultimately leading to poor cycling stability. In contrast, the electrolyte formulated with a mixture of THF and 2-MeTHF, which is characterized by a high content of AGGs (>30%) and the stable solvent 2-MeTHF as the dominant component of the solvation shell (Fig. 2f), exhibits stable long-term cycling with reversibility and stability. This system achieves an average CE of 99.91% over 400 cycles (Fig. 3d, g) without significant evolution in overpotentials, highlighting its good performance and reliability. We conducted EIS measurement to monitor solution resistance in Na||Cu half-cells containing different electrolytes. Initially, the cell with 1.0 M $NaPF_6$ in 2-MeTHF exhibited significantly higher impedance (18.52 Ω) than cells with 1.8 M $NaPF_6$ in THF (5.41 Ω) and 1.8 M $NaPF_6$ in THF/2-MeTHF (5.40 Ω), indicating lower ionic conductivity (Supplementary Fig. 10a). After 50 cycles, this resistance increased notably to 23.53 Ω for the 1.0 M $NaPF_6$ in 2-MeTHF electrolyte while remaining stable for the other two electrolytes, indicating that the difference in ionic conductivity between the electrolytes becomes more pronounced with continued cycling (Supplementary Fig. 10b).

The electrochemical behaviors of the Na negative electrode in these electrolytes become more distinct under higher current densities. Supplementary Fig. 11 compares the overpotential of Na||Na cells with the three electrolytes across current densities ranging from 1 to 6 mA/cm². Both electrolytes with pure THF or 2-MeTHF exhibit significant cell shorting at a current density of 5 mA/cm², whereas Na in 1.8 M $NaPF_6$ in THF/2-MeTHF remains stable and cycles even at 6 mA/cm². Based on these observations, a current density of 2 mA/cm² was selected to evaluate their long-term stability at high rates (Fig. 3h). At 2 mA/cm², Na in 1.8 M $NaPF_6$ in THF demonstrates a relatively low overpotential of 16.3 mV and stable Na plating/stripping for approximately 900 h. Over time, the overpotential decreases, which is likely due to an increase in the electrode surface area, before major cell shorting occurs at 1080 h (Fig. 3j). Such cell shorting raises significant safety concerns for practical applications, including the risks of fire and explosion. In the case of the 1 M $NaPF_6$ in 2-MeTHF electrolyte, the cell exhibits soft shorting from the beginning, as indicated by fluctuations in cell voltages (Fig. 3i). Initially, the overpotential gradually decreases, but it begins to increase steadily after approximately 600 h. Eventually, the cell reaches very high overpotentials, up to 140 mV, and experiences complete shorting after 800 h. This behavior suggests a lack of long-term interfacial stability, likely caused by poor transport properties at the interface. In contrast, the cell using 1.8 M $NaPF_6$ in THF/2-MeTHF electrolyte maintains a low overpotential of around 21 mV with minimal fluctuations over an extended testing period (Fig. 3h, k). The cell achieves stable Na plating and stripping for over 5000 h, demonstrating long-term stability and reliability. We further characterized the morphology of the Na metal electrode in symmetric cells after 5000 h of Na plating/stripping in 1.8 M $NaPF_6$ THF/2-MeTHF. The harvested Na electrode displayed a shiny appearance, indicating minimal side reactions with the electrolyte. Consistently, SEM images revealed highly uniform sodium deposition across both low (Supplementary Fig. 12a) and high magnifications (Supplementary Fig. 12b).

The differences in solvation structures and stability lead to distinct Na deposition morphologies on Cu substrates (Fig. 4a–c). Sodium plated from 1.8 M $NaPF_6$ in THF exhibits a grey and porous surface, indicating extensive side reactions accompanied by gas formation (Fig. 4a). This observation aligns with the low ICE of the Cu-Na cell with 1.8 M $NaPF_6$ in THF. In contrast, sodium plated from 1 M $NaPF_6$ in 2-MeTHF appears shiny, showing good stability against Na. However, the deposition is uneven with a large number of cracks, indicating inhomogeneity over a large scale (Fig. 4b). This inhomogeneity is likely due to the low ionic conductivity and limited amount of AGGs in the electrolyte. In contrast, sodium plated from 1.8 M $NaPF_6$ in THF/2-MeTHF is shiny with a smooth and compact surface (Fig. 4c).

In addition, XPS spectra reveal that while the composition of the SEI layer in the three electrolytes is similar, the relative ratios of key

components vary. In all three electrolytes, the C $1s$ spectra (Fig. 4d) show the presence of several organic components C-C/C-H, C-O, C = O, and the inorganic component Na_2CO_3. The SEI formed in 1.8 M $NaPF_6$ in THF exhibits a significantly higher content of C-C/C-H and a lower content of Na_2CO_3, suggesting more extensive solvent decomposition compared to the other two electrolytes. This observation is consistent with its porous surface morphology in Fig. 4a. Similarly, the F $1s$ spectra (Fig. 4e) and P $2p$ spectra (Fig. 4f) reveal the presence of NaF, $NaPF_6$, and Na_3PO_4 within all SEI. Among the three groups, the SEI derived from 1.8 M $NaPF_6$ in THF/2-MeTHF exhibits a significantly higher content of PF_6^-, which can be attributed to the higher concentration of AGGs with the stable solvent 2-MeTHF. The F/C and P/C ratios (Fig. 4g, h) further compare the relative content of inorganic *vs.* organic moieties in the SEIs, revealing that 1.8 M $NaPF_6$ in THF/2-MeTHF leads to the formation of an SEI with a much higher ratio of inorganic compared to the other two electrolytes throughout its depth. NaF and Na_3PO_4 (as shown in Supplementary Information Fig. 13) dominate the inner SEI composition in 1.8 M $NaPF_6$ in THF/2-MeTHF, contributing to a more passivating and stable interphase, which is consistent with the low interfacial potential observed in Na||Na cells (Supplementary Fig. 14).

Influence of solvation structure on positive electrode stability

While the negative electrode stability is primarily governed by the solvent in the cation's first solvation shell, positive electrode stability is determined by the weakly bonded free solvents. The electrochemical stability of the three electrolytes under oxidative environments was first evaluated using linear scan voltammetry (LSV) (Fig. 5a). While 2-MeTHF exhibits greater stability under reductive potentials, it is very unstable at high voltages and 1 M $NaPF_6$ in 2-MeTHF shows significant decomposition beginning at 3.4 V (cut-off current 0.01 mA/cm²). In contrast, the other two electrolytes with THF (1.8 M $NaPF_6$ in THF and THF/2-MeTHF) demonstrate good electrochemical stability above 4.5 V and as well as much lower leakage currents when held at 3.8 V (Fig. 5b), which can be attributed to their high salt concentration and the enrichment of stable THF in the free solvent state.

We further evaluated the electrochemical behaviors of these electrolytes in Na||$NaNi_{1/3}Fe_{1/3}Mn_{1/3}O_2$ (denoted as NFM) half-cells under high mass loading (14.05 mg cm⁻²) and lean electrolyte conditions (E/Active ratio = 2.5 μL/mg) (Fig. 5c, d). The positive electrode in 1 M $NaPF_6$ in 2-MeTHF electrolyte delivers a low initial capacity of 100.8 mAh g⁻¹ with a high overpotential of 172.9 mV, which can be attributed to the high charge transfer resistance in the positive electrode due to significant solvent decomposition. During 25ᵗʰ cycles, the cell exhibits rapid capacity decay, only maintaining 72.4% of its initial capacity with dramatically increased overpotentials (Fig. 5f, Supplementary Fig. 15) and decreased CEs (Supplementary Fig. 16). In contrast, the positive electrodes in the other two THF-containing electrolytes achieve a much higher initial capacity (106.8 mAh g⁻¹ for 1.8 M $NaPF_6$ in THF and 119 mAh g⁻¹ for 1.8 M $NaPF_6$ in THF/2-MeTHF) with lower overpotentials around 40 mV. The difference between these two electrolytes becomes more pronounced during long-term cycling when electrolyte consumption starts to play a significant role. After 100 cycles, the cell with 1.8 M $NaPF_6$ in THF electrolyte exhibits accelerated degradation in capacity with an increase in overpotential (Fig. 5e), ultimately leading to sudden cell failure after 190 cycles. This cell failure is primarily attributed to electrolyte depletion due to the extensive side reactions on the negative electrode side. On the other hand, the cell with 1.8 M $NaPF_6$ in THF/2-MeTHF electrolyte demonstrates a 77% capacity retention over 500 cycles with much lower evolution in overpotentials (Fig. 5g), indicating good stability at both electrodes.

Similar to the SEI, the positive electrode-electrolyte interphases (CEIs) derived from these three electrolytes have the same organic
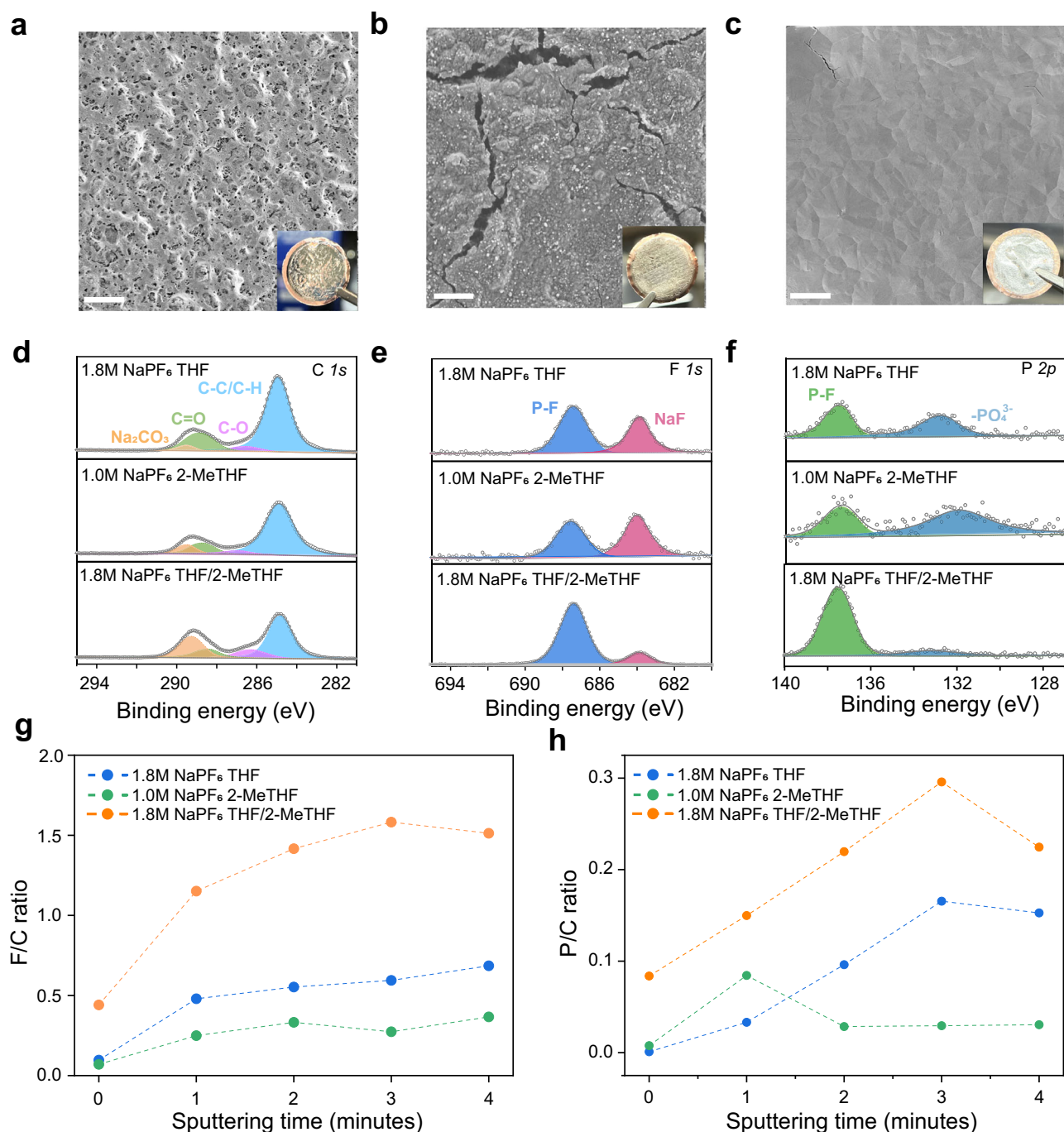
Fig. 4 | Morphology and surface compositions of Na electrodes in various electrolytes. a–c. SEM images and corresponding optical photos of Na harvested from Na∣∣Cu cells. scale bar, 10 μm. **a** 1.8 M NaPF$_6$ in THF, **b** 1 M NaPF$_6$ in 2-MeTHF and **c** 1.8 M NaPF$_6$ in THF/2-MeTHF. **d** C *1s*, **e.** F *1s* and **f.** P *2p* spectra of deposited Na surface. Statistical analyses of different atomic ratios based on XPS data collected after sputtering: **g.** F/C and **h.** P/C. The electrodes in XPS analysis were harvested from Na∣∣Cu half cells after 10 cycles under a current density of 1 mA/cm^2 with a capacity of 1 mAh/cm^2 at 22 ± 1°C.

species (C–C/C–H, C–O, C = O) and inorganic species (Na$_2$CO$_3$, NaPF$_6$, NaF, Na$_3$PO$_4$), but their relative amounts vary. Based on the C *1s* spectrum, the SEI derived in 1 M NaPF$_6$ in 2-MeTHF contains a higher percentage of C–C/C–H, which results from the decomposition of 2-MeTHF at high voltages (Fig. 5h). In comparison, SEIs in 1.8 M NaPF$_6$ in THF and 1.8 M NaPF$_6$ in THF/2-MeTHF exhibit nearly identical compositions, showing a much higher content of C-O, which can be attributed to the formation of ionic conductive sodium alkoxides (RCH$_2$ONa)[25–27]. Meanwhile, these two SEIs present a much higher content of Na$_3$PO$_4$ and NaPF$_6$ indicated by the F *1s* and P *2p* spectra (Fig. 5i, j), which explains their good positive electrode stability.

Electrochemical performance of initially anode-free sodium metal batteries

Both cycling life and calendar life are critical factors that determine the overall performance and longevity of a battery; however, achieving both simultaneously is extremely challenging[5,28,29]. Given that most of the capacity loss during battery aging primarily originates from the side reactions at the Na negative electrode, we first employed electrochemical impedance spectroscopy (EIS) to monitor the evolution of interfacial resistance (R$_{interfacial}$) of Na-Na symmetric cells with these three electrolytes. Even before storage, the EIS spectra reveal significant differences in the initial interfacial
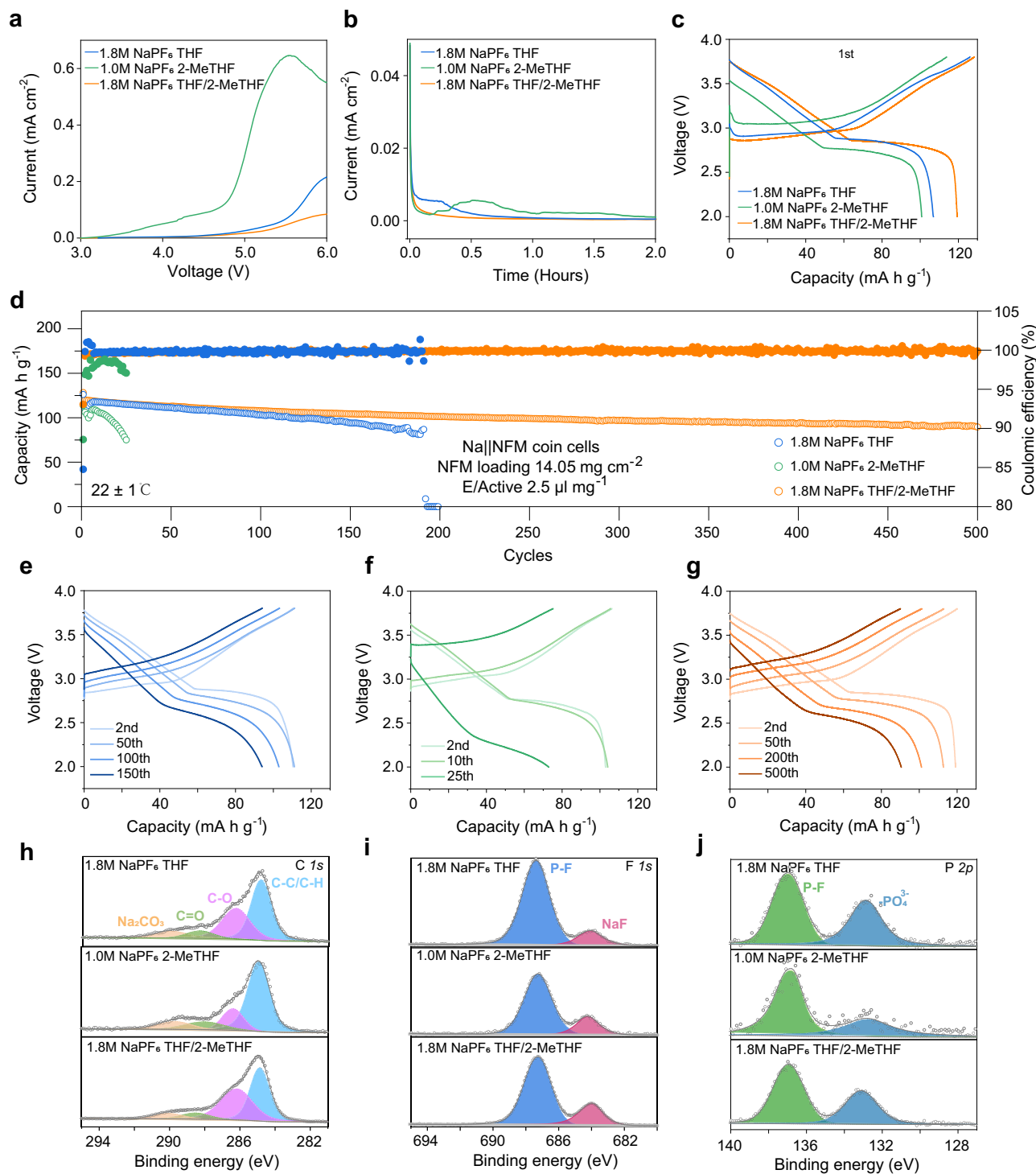
Fig. 5 | Electrochemical behavior of different electrolytes in Na‖NFM cells. **a** LSV curves measured using Al working electrodes to evaluate the electrochemical oxidation stability of different electrolytes. **b** The leakage current of Na‖Al cells with various electrolytes. **c** Voltage profiles of Na‖NFM cells during 1st cycle. **d** Long-term cycling performance and voltage profiles of Na‖NFM cells in various electrolytes, including **e** 1.8 M NaPF$_6$ in THF, **f** 1 M NaPF$_6$ in 2-MeTHF and **g** 1.8 M NaPF$_6$ in THF/2-MeTHF. **h** C *1s*, **i** F *1s* and **j** P *2p* XPS spectra of positive electrodes. The NFM electrodes in XPS analysis were harvested from Na‖NFM half cells after 10 cycles at 0.2 C-rate (1 C = 120 mA/g) at 22 ± 1°C.

resistance of Na in the various electrolytes, even after a single formation cycle, as indicated by the diameter of the semicircle in the Nyquist plot (Supplementary Fig. 17). Among these three electrolytes, the Na electrode in 1.8 M NaPF$_6$ in THF/2-MeTHF has a significantly lower interfacial resistance (3.25 Ω cm^2), compared to that in 1.8 M NaPF$_6$ in THF (8.73 Ω cm^2) and 1 M NaPF$_6$ in 2-MeTHF (24.02 Ω cm^2), indicating the formation of a thin and ionically

conductive SEI. We further monitored the evolution of interfacial resistance in these electrolytes during resting (Fig. 6a, b). The cell with 1.8 M NaPF$_6$ in THF exhibits a dramatic increase in interfacial resistance, rising from 8.73 to 18.06 Ω cm^2, representing a 2.1-fold increase over 5 days. In contrast, the cells with 1.0 M NaPF$_6$ in 2-MeTHF exhibit a 14% increase in interfacial resistance, while the cell with 1.8 M NaPF$_6$ in THF/2-MeTHF shows less than a 5% increase,
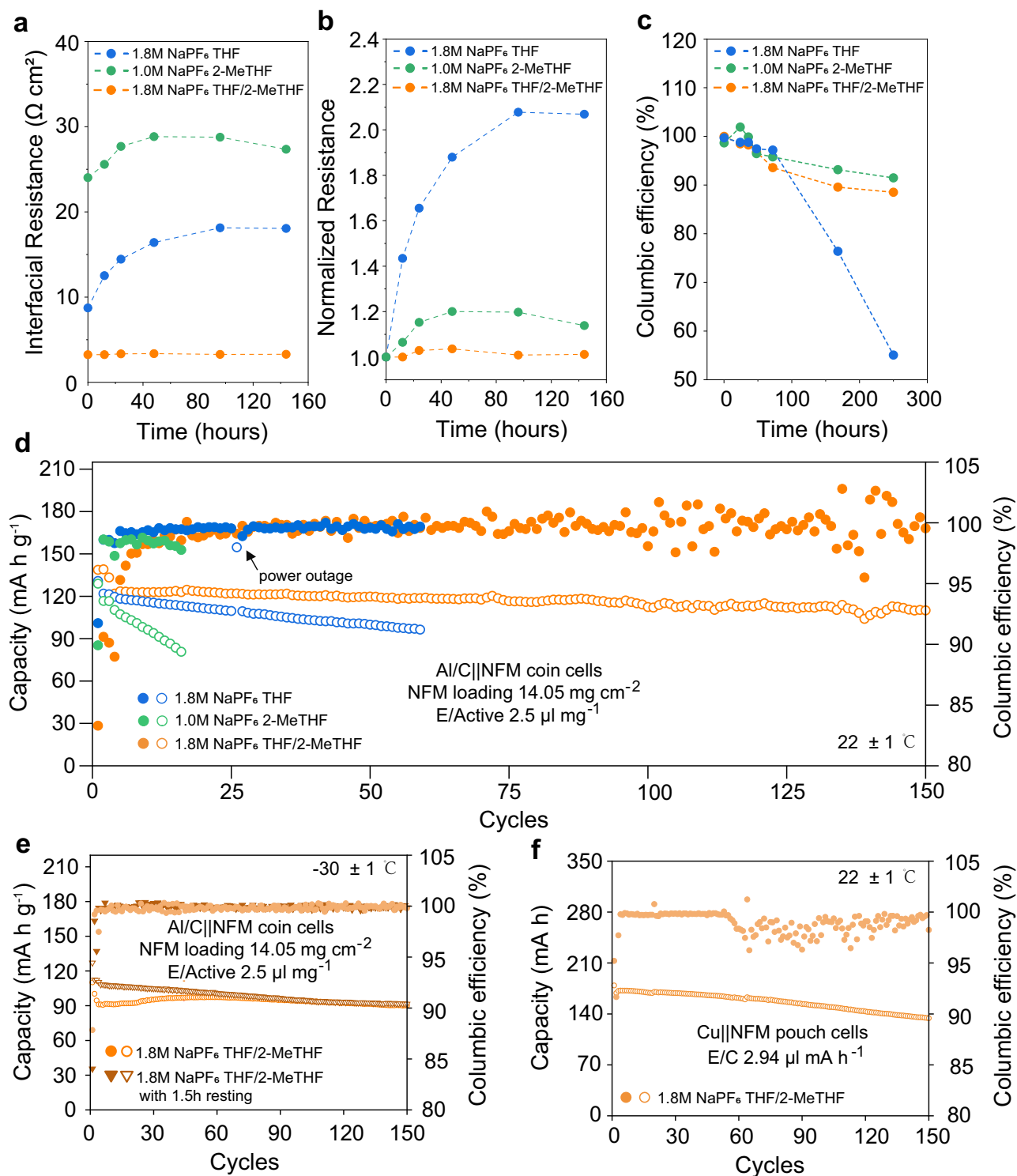
Fig. 6 | Electrochemical performance of initially anode-free sodium metal batteries with aging. a Time-dependent changes of interfacial resistance in Na||Na coin cells and **b**. normalized interfacial resistance with respect to initial resistance ($t = 0$). **c** Storage time dependence of CE of Na plating/ aging/stripping in Na||Cu coin cells. **d** The cycling performance of the Al/ C||NFM full cells with 1.5 h resting at both charged and discharged states at 22 ± 1°C. **e** the cycling performance of the Al/C||NFM full cells with the testing protocol between 2.0 V and 3.8 V, at −30 ± 1°C, charging at 0.2 C-rate and then discharging at 0.2 C-rate with and without resting for 1.5 h, 1 C = 120 mA/g. **f** Cycling performance of the initially anode-free pouch cell at 85 mA at 22 ± 1°C.

demonstrating significantly better interfacial stability. The differences in interfacial resistances and their evolution in these electrolytes highlight the critical role of presenting the electrochemically stable solvent 2-MeTHF to the Na negative electrode via AGGs to form a stable, anion-derived SEI.

The side reactions at electrochemical interfaces not only increase cell resistance but also consume the active material, ultimately shortening the battery's lifetime. To investigate how aging impacts battery lifetime, we measured the CE of Na deposition and stripping with different aging periods, ranging from 20 min to 7 days (Fig. 6c). During

the first two days, all three electrolyte systems exhibited a similarly low rate of degradation, indicating comparable initial stability. However, as the aging time extends, distinct differences emerge. Na||Cu cells with 1.0 M $NaPF_6$ in 2-MeTHF and 1.8 M $NaPF_6$ in THF/2-MeTHF electrolytes maintained a nearly constant degradation rate of 1.1%/day, reaching around 90% after 10 days of resting. In sharp contrast, the cell with 1.8 M $NaPF_6$ in THF electrolyte experienced a significant drop in CE to 76.39% at 7 days and 55.07% at 10 days, which can be attributed to the continuous side reactions at the interface and consumption of Na (Fig. 6c), which is consistent with the fast increase in interfacial resistance. Even after 21 days of storage, the cells with 1.0 M $NaPF_6$ in 2-MeTHF and 1.8 M $NaPF_6$ in THF/2-MeTHF electrolytes could still maintain a CE above 80% (Supplementary Table 15), indicating similar stability in SEI robustness. Notably, 1.8 M $NaPF_6$ in THF/2-MeTHF only contains 44 mol% of 2-MeTHF, further underscoring the crucial role of selective presentation of a stable solvent in the first solvation shell during SEI formation.

Furthermore, we evaluated the electrochemical behavior of initially anode-free Al/C||NFM cells with a high active materials mass loading of 14.05 mg cm^{-2} under low electrolyte conditions (E/Active ratio= 2.5 μL/mg). The cells were tested at 0.2 C rate (1 C = 120 mA/g) and subjected to 1.5-h resting periods at both the charged and discharged states, allowing for a comprehensive assessment of electrochemical stability under realistic operating conditions (Fig. 6d). All three cells present a similar initial capacity between 110 to 120 mAh/g, with slight variations in ICE between 80–90%. However, their capacity degradation rates varied significantly, reflecting differences in electrolyte stability at both the negative and positive electrode interfaces. The cell with 1.0 M $NaPF_6$ in 2-MeTHF showed the fastest capacity fade of 1.58% per cycle, suggesting that instability at both the negative and positive electrode contributed to continuous electrolyte decomposition and severe interfacial degradation. In contrast, the cell with 1.8 M $NaPF_6$ in THF exhibited a moderate degradation rate of 0.33% per cycle, consistent with its stability at the positive electrode but instability at the negative electrode, causing progressive capacity loss over extended cycling. Meanwhile, the cell with 1.8 M $NaPF_6$ in THF/2-MeTHF maintained the lowest degradation rate of 0.06% per cycle over 150 cycles, further supporting its stability at both the negative and positive electrode. When the resting time was further extended to 20 h, the cell with 1.8 M $NaPF_6$ in THF/2-MeTHF still maintained 83.95% capacity over 70 cycles with an average CE of 99.54% (Supplementary Fig. 18). Such good electrochemical stability also extends to low-temperature conditions. Like the 2-MeTHF based electrolytes, 1.8 M $NaPF_6$ in THF/2-MeTHF presents a low melting temperature of −67 °C, which is significantly lower than that of 1.8 M $NaPF_6$ in THF (−21 °C) (Supplementary Fig. 19). At −30 °C, 1.0 M $NaPF_6$ in 2-MeTHF and 1.8 M $NaPF_6$ in THF/2-MeTHF exhibit reversible sodium striping and plating behaviors (Supplementary Fig. 20), while 1.8 M $NaPF_6$ in THF failed to cycle due to solidification. This observation is consistent with our previous DSC results (Supplementary Fig. 19), which show that 1.8 M $NaPF_6$ in THF has a melting temperature of −21 °C. The initially anode-free cell using 1.8 M $NaPF_6$ in THF/2-MeTHF as electrolyte delivers a reversible capacity of 108 mAh g^{-1} at −30 °C, retaining 90% of its room-temperature capacity (Fig. 6e). Even with a 1.5 h resting period, it maintains a capacity of 91 mAh g^{-1} over 150 cycles, achieving 84.8% capacity retention. Furthermore, the cell exhibits wide temperature adaptability. Under alternating temperature cycling conditions (22 ± 1 °C to −30 ± 1 °C for 5 cycles each), it retains 95% of its capacity after 40 cycles (Supplementary Fig. 21), further demonstrating its robust electrochemical performance across varying temperatures. We further tested the electrolyte in a multilayer initially anode-free pouch cell with NFM positive electrodes under lean electrolyte conditions (E/C ratio=2.9 mL/Ah), which delivered an initial capacity of 171.6 mAh at 85 mA and maintained a reversible capacity of 78.17% after 150 cycles at 22 ± 1 °C (Fig. 6f). Benefiting from this design principle of

selective solvent presentation, this electrolyte of 1.8 M $NaPF_6$ in THF/2-MeTHF enables the stable cycling of initially anode-free sodium metal batteries, presenting low degradation rate of 0.06%/cycle in coin cells and 0.15%/cycle in pouch cell, which are the lowest among literature (Supplementary Table 16). These results highlight the practical application potential of 1.8 M $NaPF_6$ in THF/2-MeTHF for next-generation Na metal batteries, particularly in all temperature conditions, such as electric vehicle applications and electric power grids. This electrolyte design principle of selective solvent presentation is proposed and demonstrated here for the first time, but there are previous electrolyte combinations that inadvertently fall into this category, such as LiD-FOB/EM/EA electrolyte[30] and LiClO₄/DME/PC electrolyte for Li-ion batteries[31] and LiFSI/6FDMH/DME for Li-metal batteries[32].

Discussion

In summary, we have demonstrated an electrolyte design approach that selectively directs solvent presentation at the negative and positive electrode interfaces separately. This strategy fundamentally distinguishes determinants of electrode stability: negative electrode stability is governed by solvents in the cation's first solvation shell, while positive electrode stability depends on weakly bonded free solvents. By implementing this concept, we enriched the negative electrode-stabilizing solvent 2-methyltetrahydrofuran in the first solvation shell and positive electrode-stabilizing solvent tetrahydrofuran in the weakly bonded state, resulting in an electrolyte with electrochemical stability against both electrodes. The selective solvent presentation strategy provides a rational framework for optimizing solvation structures, addressing the distinct electrochemical needs of both electrodes. This approach paves the way for the development of initially anode-free metal batteries, particularly in sodium-, lithium-, and potassium-based energy storage systems.

Methods

Electrodes and electrolytes

Sodium hexafluorophosphate ($NaPF_6$) (MSE Supplies LLC, Purity > 99.9%) was used as received. Tetrahydrofuran (THF) (Sigma-Aldrich, Purity > 99.9%, anhydrous, inhibitor-free) and 2-methyltetrahydrofuran (2-MeTHF) (Sigma-Aldrich, Purity > 99%, anhydrous, inhibitor-free) were used as received. The single-side coated layered oxide $NaNi_{1/3}Fe_{1/3}Mn_{1/3}O_2$ positive electrodes purchased from MTI Corporation and dried over night before using. The detailed information on the electrode is shown in Supplementary Table 17. Copper foils (MTI corporation, 25 μm thickness, ≥99.8% purity) were used in Na||Cu half cells. High-purity sodium chips (MTI corporation, 15.6 mm in diameter, 0.45 mm thickness, total capacity of 97.23 mAh) were used in Na||NFM half cells, Na||Cu half cells, and Na||Na symmetric cells. Amorphous carbon (MTI corporation, 16 μm thickness) coated on aluminum foil was used as negative electrodes for the initially anode-free full cell. The solution of 1.8-M $NaPF_6$ in 1:1 (vol.: vol.) THF and 2-MeTHF was used as the electrolyte.

Electrochemical testing

For all coin cells (CR2032 coin-type cells), the case and spring are made of 304 stainless steel. All Na||Cu and Na||Na cells were assembled in an argon-filled glovebox with an O_2 level < 0.2 ppm and an H_2O level < 0.01 ppm, with two pieces of Celgard 2400 (porosity: 41%, diameter: 20 mm, thickness: 25 μm) and one piece of Whatman GF/D (pore size: 2.7 μm, porosity: 40–50%, diameter: 20 mm, thickness: 0.68 mm) as the separators and 100 μL electrolytes. Na||NFM and Al/C||NFM full cells were assembled with just one piece of Celgard 2325 (porosity: 39%, diameter: 20 mm, thickness: 25 μm) and 40 μL electrolytes. All cells were held at open-circuit voltage for 12 h prior to electrochemical measurements. Galvanostatic charge–discharge experiments on coin cells were carried out using Land 8-channel battery testers, while other electrochemical testing

was conducted with a Biologic VMP3 system. Na||NFM and Al/C||NFM cells were cycled within 2.0–3.8 V. C-rates and specific capacities were calculated relative to the mass loading of the NFM active materials. Dry Cu||NFM 402035 pouch cells with a capacity around 170 mAh were purchased from Li-Fun Technology and used as received. 0.5 mL of electrolyte was used in each cell (E/C = 2.9 mL/Ah), and the cells were vacuum-sealed at −90 kPa using an MSK-115A (MTI corporation) vacuum sealer. The pouch cells were rested at the open-circuit voltage for 24 h and went through two formation cycles under a current of 20 mA. An initial pressure of ~30 psi is applied to pouch cells prior to cycling, and the cells were subsequently cycled under constant-gap conditions. Long-term cycling stability test was conducted at 85 mA between 2–3.8 V. The cyclic voltammetry tests were carried out over a voltage range of −0.2 to 1.5 V for Na||Cu cells with 5 mV/s under 25 ± 1 °C and -30 ± 1 °C. EIS was performed with an applied AC potential of 10 mV in the frequency range of 1 MHz to 0.01 Hz at 22 ± 1 °C.

Characterizations

The morphology investigation was performed with SEM (SEM Zeiss Gemini SEM 450) operated at 20 kV. The SEM samples were harvested from Na||Cu half cells after one formation cycle at a current density of 0.5 mA cm^{-2} for 2 h and following by a metal deposition step at 1 mA cm^{-2} for 4 h to ensure a complete coverage of Cu substrate. The samples were washed with corresponding electrolyte solvents and dried in the Ar-filled glovebox at 22 ± 1 °C before being transferred to the SEM chamber for imaging. During sample transfer process, there was air exposure for less than 1 s, which we believe did not significantly change the morphology of Na deposits. XPS analysis was performed with a Thermo K alpha X-ray Photoelectron Spectrometer at 22 ± 1 °C, coin cells were cycled, the Cu electrodes were obtained by disassembling the Na||Cu cells inside an Ar-filled glove box, washed with relative solvents and dried inside the glove box. All samples were transferred to characterization instruments using inert atmosphere sample holders to prevent oxidation. Ar ion sputtering was employed for the depth profile analysis. A sputtering with a power of 4 kV × 0.5 mA on a 2 mm × 2 mm surface was deployed. The ionic conductivities of the electrolytes at 25 °C were measured with a SevenCompact S230 Conductivity Benchtop Meter. NMR spectroscopy was performed via Artemis–Bruker Avance-400. The Differential scanning calorimetry (DSC TA Q100) tests were performed at a heating rate of 5 °C min^{-1} under the Ar atmosphere. Raman spectra were performed on a Horiba LabRAM HR Evolution Raman Spectrometer with a range of 600–1200 cm^{-1} at 25 ± 1 °C.

Molecular dynamics simulation parameters

Atomistic MD simulations were performed in the isothermal-isobaric ensemble using GROMACS 2021. Solvent molecules were parameterized using the OPLS-AA force field, while parameters for Na$^+$ and PF$_6^-$ were taken from the OPLS-2009IL force field with their total charges scaled to ±0.8e to simulate polarization effects[33]. Specifically, all partial charges on PF$_6^-$ were uniformly scaled to yield a net charge of −0.8e, and the Na$^+$ charge was adjusted to +0.8e to maintain overall charge neutrality. No charge rescaling was applied to the solvent molecules (THF and 2-MeTHF), and all Lennard-Jones parameters remained unchanged. While charge scaling may attenuate short-range RDF peak intensities[33], previous studies have shown that this approach improves the accuracy of solvation structure and transport properties in similar electrolyte systems[18,34–37]. Additionally, the specific combination of OPLS-AA parameters and charge-scaled ionic liquid parameters in this work has been validated and used in recent studies of electrolyte solvation structure[19,38,39]. Each simulation system was initialized with a cubic box containing the specified number of molecules listed in Supplementary Table 3. The systems were first

energy-minimized and then equilibrated for 10 ps in the NVT ensemble at 298.15 K using a velocity-rescale thermostat with a 1.0 ps time constant. This equilibration was followed by a 50 ns equilibration in the NPT ensemble at 298.15 K and 1 bar using a velocity-rescale thermostat and a stochastic cell rescaling barostat with a 5.0 ps time constant and an isothermal compressibility of 4.5×10^{-5} bar^{-1}. Finally, a 50 ns production simulation was conducted in the NPT ensemble, maintaining the same temperature, pressure, thermostat, and barostat settings as used during the preceding NPT equilibration. The stability of the solvation structure for this simulation time was confirmed by tracking Na−P and Na−O coordination numbers over the production trajectory, which remained stable over time (Supplementary Fig. 25, Supplementary Note 3). All simulations were conducted using the leapfrog integrator with a 2-fs timestep. A Verlet cutoff scheme was employed with a neighbor list cutoff of 1.3 nm. Van der Waals interactions were modeled using a shifted Lennard-Jones potential that smoothly transitioned to zero at 1.3 nm. Standard long-range dispersion corrections to energy and pressure were applied. Electrostatic interactions were calculated with the Particle Mesh Ewald (PME) method with a short-range cut-off of 1.3 nm, a grid spacing of 0.12 nm, and 4th-order interpolation. Two simulation replicas were performed for each system to quantify simulation error. Both replicas were initialized from the same atomic configuration, then separate NVT and NPT equilibration and production simulations were performed using different random seeds.

Molecular dynamics simulation analysis

Time-averaged ion distributions within each cation solvation shell were analyzed based on the number of PF$_6^-$ anions (counted based on the number of phosphorus atoms) within 0.5 nm of each Na$^+$ cation. This distance cutoff was selected based on the location of the first peak in the RDF between Na$^+$ and any other atom. To test the robustness of this approach, we conducted a sensitivity analysis using alternative cutoff values of 0.4 nm and 0.6 nm. As shown in Supplementary Table 6, these variations had a negligible effect on the N(r) and did not affect the overall speciation trends. Each solvation shell was classified into one of five types based on the number of phosphorus atoms (P) it contained: solvent-separated ion pair (SSIP) for $P = 0$, contact ion pair (CIP) for $P = 1$, and aggregates for $P \geq 2$. (Supplementary Fig. 4) Time-averaged percentages of THF *vs.* 2-MeTHF molecules within the cation solvation shells were also computed for each type of solvation shell by calculating the number of THF and 2-MeTHF molecules surrounding each Na$^+$ ion using the same distance cut-off.

Data availability

The authors declare that the main data supporting our findings of this study are contained within the paper and Supplementary Information. The source data generated in this study are provided in the Source Data file. Molecular simulation data, including input and output data files, simulation configurations, and simulation trajectories, generated in this study have been deposited in the Dryad repository[40]. Source data are provided with this paper.

Code availability

Code utilized to analyze molecular simulation trajectories has been deposited alongside the source data in the Dryad repository[40], is available under the CC0 license, and can be accessed without restriction.

References

1. Chen, Y. et al. Prospects for practical anode-free sodium batteries. *Mater. Today* **73**, 260–274 (2024).
2. Cohn, A. P. et al. Anode-free sodium battery through in situ plating of sodium metal. *Nano Lett.* **17**, 1296–1301 (2017).

3. Sun, B. et al. Design strategies to enable the efficient use of sodium-metal anodes in high-energy batteries. *Adv. Mater.* **32**, 1903891 (2019).

4. Yang, T. et al. Anode-free sodium metal batteries as rising stars for lithium-ion alternatives. *iScience* **26**, 105982 (2023).

5. Boyle, D. T. et al. Corrosion of lithium metal anodes during calendar ageing and its microscopic origins. *Nat. Energy* **6**, 487–494 (2021).

6. Sun, Y. et al. Wide-temperature-range sodium-metal batteries: from fundamentals and obstacles to optimization. *Energy Environ. Sci.* **16**, 4759–4811 (2023).

7. Huang, Z. et al. A comprehensive review on liquid electrolyte design for low-temperature lithium/sodium metal batteries. *Energy Environ. Sci.* **17**, 5365–5386 (2024).

8. Hu, L. et al. Restructuring electrolyte solvation by a versatile diluent toward beyond 99.9% coulombic efficiency of sodium plating/stripping at ultralow temperatures. *Adv. Mater.* **36**, 2312161 (2024).

9. Vaidyula, R. et al. Binary solvent induced stable interphase layer for ultra-long life sodium metal batteries. *Adv. Mater.* **36**, 202312508 (2024).

10. Wang, C. et al. Extending the low-temperature operation of sodium metal batteries combining linear and cyclic ether-based electrolyte solutions. *Nat. Commun.* **13**, 4934 (2022).

11. Wang, S. et al. An ultrastable low-temperature Na metal battery enabled by synergy between weakly solvating solvents. *J. Am. Chem. Soc.* **146**, 3854–3860 (2024).

12. Chen, L. et al. Dynamic shielding of electrified interface enables high-voltage lithium batteries. *Chem* **10**, 1196–1212 (2024).

13. Parejo-Tovar, A. et al. Operando tracking of ion population changes in the EDL electrode of a lithium-ion capacitor during its charge/discharge. *Energy Storage Mater.* **73**, 103810 (2024).

14. Chen, S. et al. Challenges and recent progress on anodes and their interfacial optimization towards high-performance rechargeable magnesium batteries. *Mater. Today* **72**, 282–300 (2024).

15. Gupta, S. et al. Aluminum batteries: opportunities and challenges. *Energy Storage Mater.* **70**, 103538 (2024).

16. Goldman, J. L. et al. Structure-reactivity relationships of methylated tetrahydrofurans with lithium. *J. Electrochem. Soc.* **127**, 1461 (1980).

17. Yao, N. et al. Applying classical, ab initio, and machine-learning molecular dynamics simulations to the liquid electrolyte for rechargeable batteries. *Chem. Rev.* **122**, 10970–11021 (2022).

18. Self, J. et al. Transport in superconcentrated $LiPF_6$ and $LiBF_4$/propylene carbonate electrolytes. *ACS Energy Lett.* **4**, 2843–2849 (2019).

19. Zheng, X. et al. Knocking down the kinetic barriers towards fast-charging and low-temperature sodium metal batteries. *Energy Environ. Sci.* **14**, 4936–4947 (2021).

20. Hu, J. et al. Understanding the solvation-dependent properties of cyclic ether multivalent electrolytes using high-field NMR and quantum chemistry. *JACS Au* **2**, 917–932 (2022).

21. Yu, Z. et al. Rational solvent molecule tuning for high-performance lithium metal battery electrolytes. *Nat. Energy* **7**, 94–106 (2022).

22. Zou, Y. et al. Electrolyte solvation engineering stabilizing anode-free sodium metal battery with 4.0 V-class layered oxide cathode. *Adv. Mater.* **36**, 2410261 (2024).

23. Wang, F. et al. Highly reversible zinc metal anode for aqueous batteries. *Nat. Mater.* **17**, 543–549 (2018).

24. Wang, S. et al. Unraveling the solvent effect on solid-electrolyte interphase formation for sodium metal batteries. *Angew. Chem. Int. Ed.* **62**, e202313447 (2023).

25. Zhang, J. et al. Achieving superb sodium storage performance on carbon anodes through an ether-derived solid electrolyte interphase. *Energy Environ. Sci.* **10**, 370–376 (2017).

26. Li, K. et al. Evolution of the electrochemical interface in sodium ion batteries with ether electrolytes. *Nat. Commun.* **10**, 725 (2019).

27. Wang, C. C. et al. Bulk bismuth as a high-capacity and ultralong cycle-life anode for sodium-ion batteries by coupling with glyme-based electrolytes. *Adv. Mater.* **29**, 1702212 (2017).

28. Li, G. X. et al. Enhancing lithium-metal battery longevity through minimized coordinating diluent. *Nat. Energy* **9**, 817–827 (2024).

29. Kwon, H. et al. Borate–pyran lean electrolyte-based Li-metal batteries with minimal Li corrosion. *Nat. Energy* **9**, 57–69 (2024).

30. Li, et al. A new strategy for sulfone-containing electrolytes design enabling long cycling high-voltage lithium-ion batteries. *Adv. Funct. Mater.* **35**, 241687 (2025).

31. Wang, H. et al. Dual-solvent Li-ion solvation enables high-performance Li-metal batteries. *Adv. Mater.* **33**, 2008619 (2021).

32. Chen et al. Identifying the Role of solvation entropy for the solvation chemistry in non-aqueous electrolytes. *Angew. Chem. Int. Ed.* **64**, e202501315 (2025).

33. Doherty, B. et al. Revisiting OPLS force field parameters for ionic liquid simulations. *J. Chem. Theory Comput.* **13**, 6131–6145 (2017).

34. Cui, X. et al. High-voltage Li metal batteries enabled by a non-flammable amphiphilic electrolyte. *Energy Storage Mater.* **66**, 103235 (2024).

35. Hakim, L. et al. Transport properties of ionic liquid and sodium salt mixtures for sodium-ion battery electrolytes from molecular dynamics simulation with a self-consistent atomic charge determination. *J. Phys. Chem. B* **124**, 7291–7305 (2020).

36. Mistry, A. et al. Toward bottom-up understanding of transport in concentrated battery electrolytes. *ACS Central Sci.* **8**, 880–890 (2022).

37. Gerlitz, A. I. et al. Polypropylene carbonate-based electrolytes as model for a different approach towards improved ion transport properties for novel electrolytes. *Phys. Chem. Chem. Phys.* **25**, 4810–4823 (2023).

38. Ma, B. et al. Molecular-docking electrolytes enable high-voltage lithium battery chemistries. *Nat. Chem.* **16**, 1427–1435 (2024).

39. Zhang, W. et al. Engineering a passivating electric double layer for high performance lithium metal batteries. *Nat. Commun.* **13**, 2029 (2022).

40. Xing, Q. et al. Directing Selective Solvent Presentations at Electrochemical Interfaces to Enable Initially Anode-Free Sodium Metal Batteries, Dryad, https://doi.org/10.5061/dryad.9w0vt4btn (2025).

Acknowledgements

Author contributions

Q.X. and F.L. conceived the idea. Q.X. performed electrolyte preparations, the NMR, Raman, cell fabrication, and electrochemical testing, and drafted the paper. Z.Y. performed the SEM, XPS experiments, and corresponding analysis. J.M.L. and R.C.V. performed the MD simulations and corresponding analysis. F.L. supervised the project and revised the manuscript. All authors discussed the results and provided feedback to the manuscript.

Competing interests

The authors declare no competing interests.

Additional information

Supplementary information The online version contains supplementary material available at
https://doi.org/10.1038/s41467-025-63902-4.

Correspondence and requests for materials should be addressed to Fang Liu.

Peer review information *Nature Communications* thanks Jiarui He, and the other, anonymous, reviewer(s) for their contribution to the peer review of this work. A peer review file is available.

Reprints and permissions information is available at http://www.nature.com/reprints

Publisher's note Springer Nature remains neutral with regard to jurisdictional claims in published maps and institutional affiliations.